

Article

Strong and Hierarchical Ni(OH)₂/Ni/rGO Composites as Multifunctional Catalysts for Excellent Water Splitting

Lixin Wang¹, Ailing Song^{2,3,*} , Yue Lu², Manman Duanmu², Zhipeng Ma^{2,3}, Xiujuan Qin^{2,*} and Guangjie Shao^{2,3} 

- ¹ Shijiazhuang Key Laboratory of Low Carbon Energy Materials, College of Chemical Engineering, Shijiazhuang University, Shijiazhuang 050035, China; 1902003@sjzc.edu.cn
- ² Hebei Key Laboratory of Applied Chemistry, College of Environmental and Chemical Engineering, Yanshan University, Qinhuangdao 066004, China; yueluysu@stumail.ysu.edu.cn (Y.L.); manman.duanmu@stumail.ysu.edu.cn (M.D.); mazp@ysu.edu.cn (Z.M.); shaoguangjie@ysu.edu.cn (G.S.)
- ³ State Key Laboratory of Metastable Materials Science and Technology, Yanshan University, Qinhuangdao 066004, China
- * Correspondence: ailing.song@ysu.edu.cn (A.S.); qinxj@ysu.edu.cn (X.Q.)

Abstract: The lack of efficient and non-precious metal catalysts poses a challenge for electrochemical water splitting in hydrogen and oxygen evolution reactions. Here, we report on the preparation of growing Ni(OH)₂ nanosheets in situ on a Ni and graphene hybrid using supergravity electrodeposition and the hydrothermal method. The obtained catalyst displays outstanding performance with small overpotentials of 161.7 and 41 mV to acquire current densities of 100 and 10 mA cm⁻² on hydrogen evolution reaction, overpotentials of 407 and 331 mV to afford 100 and 50 mA cm⁻² on oxygen evolution reaction, and 10 mA·cm⁻² at a cell voltage of 1.43 V for water splitting in 1 M KOH. The electrochemical activity of the catalyst is higher than most of the earth-abundant materials reported to date, which is mainly due to its special hierarchical structure, large surface area, and good electrical conductivity. This study provides new tactics for enhancing the catalytic performance of water electrolysis.

Keywords: water splitting; hierarchical architecture; nickel hydroxide; Ni-based electrode; electrocatalytic activity



Citation: Wang, L.; Song, A.; Lu, Y.; Duanmu, M.; Ma, Z.; Qin, X.; Shao, G. Strong and Hierarchical Ni(OH)₂/Ni/rGO Composites as Multifunctional Catalysts for Excellent Water Splitting. *Catalysts* **2024**, *14*, 309. <https://doi.org/10.3390/catal14050309>

Academic Editor: Bruno Fabre

Received: 27 March 2024

Revised: 27 April 2024

Accepted: 30 April 2024

Published: 7 May 2024



Copyright: © 2024 by the authors. Licensee MDPI, Basel, Switzerland. This article is an open access article distributed under the terms and conditions of the Creative Commons Attribution (CC BY) license (<https://creativecommons.org/licenses/by/4.0/>).

1. Introduction

With fossil fuel consumption and the increasing demand and supply of energy, it has become a dominant trend to discover novel technologies used for clean and scalable energy substitutes [1–4]. Recently, electrochemical water splitting for hydrogen and oxygen fuel has drawn much attention to reduce overpotential and enhance the reaction rate [5–7]. The Pt-based system is the most advanced catalyst for hydrogen evolution reaction (HER), and RuO₂ and IrO₂ catalysts present the supreme performance for oxygen evolution reaction (OER) [8–10]. Nonetheless, these kinds of precious metal catalysts are limited in their applications because of their high price, scarcity, and low bifunctional activities [11,12]. Therefore, designing an eco-friendly and energy-saving catalyst for water reduction and oxidation in a cathode and anode is very urgent [13–16].

Recently, non-noble metal materials such as HER or OER electrocatalysts have been researched broadly. Moreover, there is no doubt that Ni-based and Ni hydroxide catalysts among these materials have drawn much interest in terms of exploring their outstanding electrocatalytic performances on HER and OER [17–20]. For example, Yin et al. reported a facile wet-chemical method to grow ultrathin one-dimensional Pt nanowires in situ on single-layered 2D Ni(OH)₂ nanosheets. The hybrid materials exhibit high electrocatalytic activity for HER in an alkaline solution, 4–5 times higher than the commercial Pt/C catalyst [20]. Gao et al. reported the simple synthesis and use of Ni(OH)₂ nanocrystals as

a remarkably active and stable OER catalyst in alkaline media [21]. Li et al. successfully synthesized NiSe@NiOOH core-shell hyacinth-like nanostructures supported on nickel foam by a facile solvothermal selenization and subsequent in situ electrochemical oxidation. The electrochemical performance of NiSe@NiOOH/NF for OER was investigated [22]. Li et al. synthesized a delicate NiCo(OH)_x-Co_yW catalyst with a bush-like heterostructure via gas-template-assisted electrodeposition and an electrochemical etching-growth process, which ensured a high active area and fast gas release kinetics for HER [23]. Zhang et al. synthesized Ni@Ni(OH)₂ core-shell nanomaterials through molten salt polymerization. Ni(OH)₂ was coated on the Ni core to make the catalyst monomer adsorb H* and OH* simultaneously, forming good hydrogen chemical kinetics and improving the catalytic stability of the catalyst [24].

The documents mentioned above describe the application of Ni-based materials and Ni hydroxides on HER or OER. Furthermore, many significant studies are concerned with bifunctional catalysts. Jia et al. reported a heterostructured catalyst by coupling an exfoliated Ni-Fe layered double-hydroxide nanosheet and defective graphene. The catalyst has exhibited extremely high electrocatalytic activity for HER and OER in an alkaline solution [25]. Liu et al. have successfully synthesized nickel oxysulfide fullerene-like hollow nanospheres grown in situ on 3D nickel foams as a kind of efficient bifunctional electrocatalyst in strongly alkaline electrolytes, which could be attributed to the synergetic effect of the proper ratios of sulfur and oxygen [26]. Rao et al. synthesized hydrotalcite-like Ni(OH)₂ nanosheets grown on Ni foam via a facile one-pot hydrothermal method. The resultant Ni(OH)₂/NF electrode shows superior electrocatalytic activity and durability for HER and OER, as well as overall water splitting [27]. Yang et al. prepared NiP₂/NiSe₂ porous precursor on carbon fiber cloth by simple hydrothermal reaction using nickel nitrate and obtained the basic product with good morphology. It is well applied to HER, OER, and overall water splitting [28]. Wu et al. reported the modulation of metallic Mo₂S₃ and in situ epitaxial growth of bifunctional Ni-based catalyst (Mo₂S₃@NiMo₃S₄) to construct a metallic heterostructure which can facilitate the charge transfer for water splitting [29].

According to the analysis of the above examples, it can be seen that the composite materials of Ni hydroxides and Ni-based metals exhibit good performance in water splitting. This is caused by the fact that Ni hydroxides are inclined to cleave the HO–H bond for dissociation of water, but are inefficient for converting the produced hydrogen intermediates (H_{ads}) into H₂. On the contrary, most Ni-group metals benefit from the adsorption and recombination of the H_{ads}, yet they are commonly incompetent in cleaving the HO–H bond. Therefore, according to their respective electrochemical characteristics, we can combine the catalytic advantages of Ni hydroxides and Ni-based metals to design an excellent composite electrocatalyst on both HER and OER.

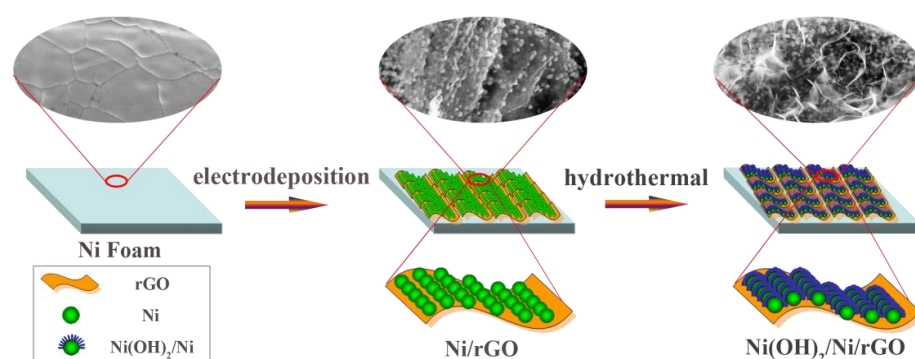
In this paper, we prepared a hierarchical Ni(OH)₂/Ni/rGO composite electrode, the main steps of which are as follows: First, a foamed nickel substrate subjected to ultrasonication and acidification was used as an electrodeposited cathode, and a Ni/rGO composite electrode was prepared by supergravity electrodeposition, which has been reported in our previous paper [30]. Then, the Ni nanoparticles on the surface of the Ni/rGO electrode were reacted with urea via the hydrothermal method, and a layer of Ni(OH)₂ nanoplates was vertically grown in situ on the surface of the Ni particles. The resulting Ni(OH)₂/Ni/rGO electrodes have a unique tertiary structure. The primary structure is a Ni foam substrate. The Ni foam has a three-dimensional and porous architecture, increasing the surface area of the composite electrode and ensuring that the electrolyte or gas can pass through unimpededly. The secondary structure is the Ni/rGO part, and the rGO layers are interconnected to form a 3D-networked frame on which plenty of Ni nanoparticles are uniformly supported. In addition, the tertiary structure is Ni(OH)₂ nanosheets. Based on the results, the aim of this study is to combine the different catalytic characteristics of Ni and Ni(OH)₂ to create a new bifunctional metal–metal hydroxide system with excellent and stable HER and OER performances. Furthermore, the impact of urea concentration on the morphology, microstructure, and electrocatalytic properties of the composite electrodes was elaborately researched. We

foretell that this study can provide a fresh perspective on non-precious metals as bifunctional electrocatalysts, which is attributed to their unique hierarchical structure, large specific surface area, good electrical conductivity, and synergistic effect between Ni and Ni(OH)₂.

2. Results and Discussions

2.1. Morphology Analysis

The flow chart for a synthetic process of the hierarchical Ni(OH)₂/Ni/rGO composite catalyst is obtained by two experimental steps (Scheme 1). The Ni/rGO composite electrode was fabricated via supergravity electrodeposition [30], which converted Ni ions in a plating solution into Ni nanoparticles grown in situ on rGO layers. The interconnected rGO layers are key in refining Ni particles and conducting electricity. In another hydrothermal process, Ni nanoparticles directly provide a Ni source that reacts with urea and forms Ni(OH)₂ nanosheets on the surface of Ni particles. The obtained Ni(OH)₂/Ni/rGO catalyst has a hierarchical architecture. To our knowledge, Ni foam possesses a special porous structure, making it more conducive to transferring gases and electrolytes and improving their electrocatalytic properties. Hence, the Ni foam substrate acts as the first structure. In addition, the secondary structure is the Ni/rGO hybrid, and the tertiary structure is the Ni(OH)₂ nanosheets grown in situ vertically on Ni particles.



Scheme 1. The flow chart for hierarchical Ni(OH)₂/Ni/rGO composite catalyst preparation process.

Figure S1 presents the pristine Ni foam substrate with a 3D macroporous morphology and smooth surface. Figure S2 presents a high-magnification SEM image of a prepared Ni/rGO catalyst. It shows that rGO layers form an interconnected texture on which lots of Ni nanoparticles are uniformly loaded. The low-magnification SEM image of the Ni(OH)₂/Ni/rGO-1 cathode reveals that the surface of the Ni foam is entirely covered with the Ni(OH)₂/Ni/rGO hybrid, as shown in Figure S3. As displayed in Figure 1a,b, the high-magnification SEM image of Ni(OH)₂/Ni/rGO-1 further displays that the Ni(OH)₂ nanosheets grow vertically in situ on the surface of the Ni particles and form a staggered structure. In this process, Ni nanoparticles act as a source of nickel and do not require adding a new nickel source. These Ni(OH)₂ nanosheets present an average size of about ~10 nm with the thickness displayed in Figure S4. And the surface size of Ni(OH)₂ nanosheets is about 5–500 nm. Furthermore, the elemental mappings (Figure S5a–c) demonstrate the existence of C, O, and Ni elements, which is also in good accordance with the EDS analysis (Figure S5d) of the Ni(OH)₂/Ni/rGO-1 hybrid catalyst. The atom ratios of C, O, and Ni in the Ni(OH)₂/Ni/rGO-1 coating are 58.81 at%, 14.85 at% and 26.34 at%, respectively. As revealed in Figure 1c,d, the SEM image of the Ni(OH)₂/Ni/rGO-2 catalyst shows that a small fraction of Ni(OH)₂ nanoflakes disappear and Ni nanoparticles are exposed. As the concentration of urea increases during the hydrothermal process, more and more Ni(OH)₂ nanoflakes disappear, and more and more Ni particles are exposed as displayed in Figure 1e–g. When the urea concentration reaches 40 mg mL^{−1}, all Ni(OH)₂ nanoflakes disappear, and the Ni particles and rGO layers are completely exposed, as displayed in Figure 1h. After the hydrothermal process, the color of the urea solution changes obviously, as displayed in Figure S6. As the concentration of urea increases in the hydrothermal

process, the solution color changes from colorless to dark blue, which is attributed to more and more Ni ions dissolving in the solution from the falling of the $\text{Ni}(\text{OH})_2$ nanoflakes. Figure 2a shows a TEM image of the Ni/rGO coating. Ni nanoparticles are uniformly dispersed on the rGO layers. The surface of the Ni nanoparticles is smooth and the sizes of the Ni particles are about 300 nm. As shown in Figure 2b, TEM analysis displays a mass of $\text{Ni}(\text{OH})_2$ nanosheets which spalled off the $\text{Ni}(\text{OH})_2/\text{Ni}/\text{rGO}$ -1 coating with a 1 h sonicated treatment. Figure 2c shows the hybrid is spalled off the $\text{Ni}(\text{OH})_2/\text{Ni}/\text{rGO}$ -3 coating, which shows that the sizes of Ni nanoparticles are about 200 nm, and some $\text{Ni}(\text{OH})_2$ flakes are detached from the surface of Ni particles. Figure 2d shows the $\text{Ni}(\text{OH})_2/\text{Ni}/\text{rGO}$ -5 catalyst. The $\text{Ni}(\text{OH})_2$ flakes seem to disappear completely, and the edges of the Ni particles become serrated. This phenomenon is because $\text{Ni}(\text{OH})_2$ nanosheets are detached from the surface of the Ni particles and dissolved in the urea solution. And this is the reason why the solution is dark blue in the container when the urea concentration becomes larger. All of the above discoveries strongly favor the successful growth of $\text{Ni}(\text{OH})_2$ nanoflakes on Ni/rGO surface merely via one-pot hydrothermal preparation in the urea solution.

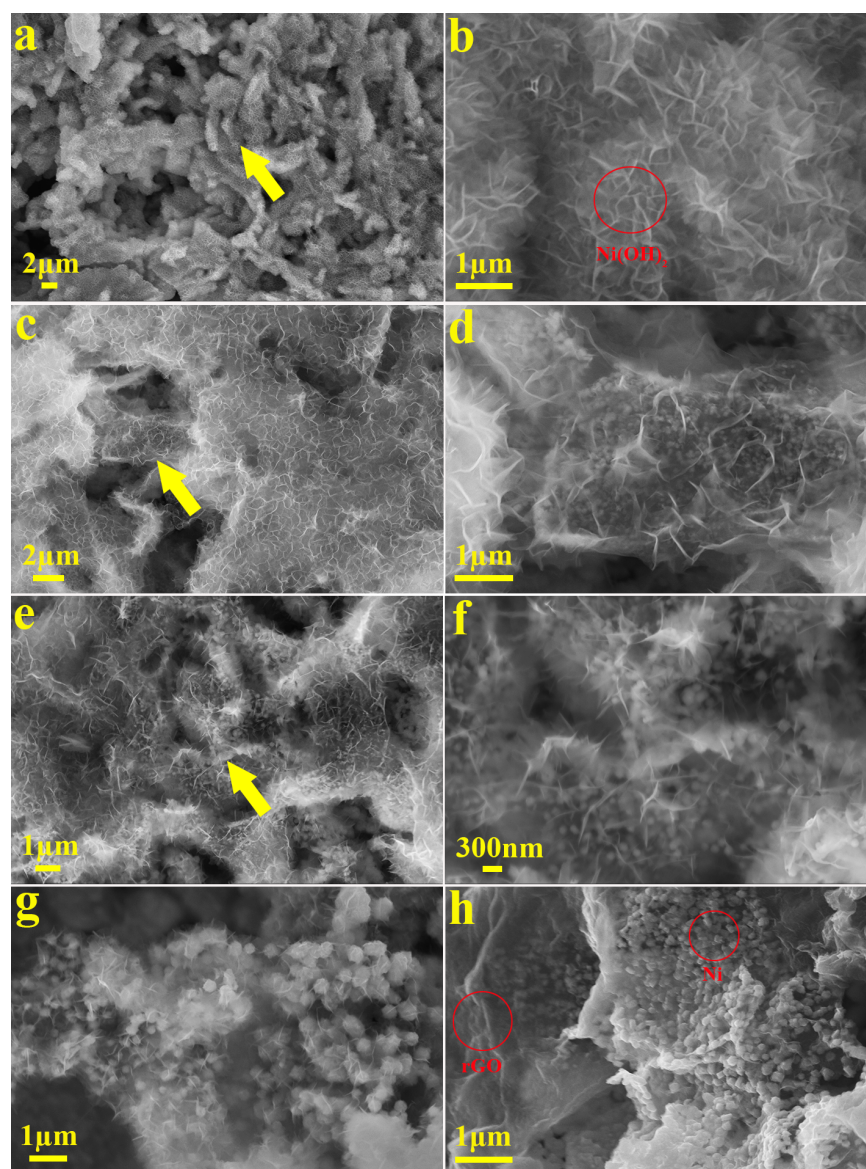


Figure 1. SEM images of (a,b) $\text{Ni}(\text{OH})_2/\text{Ni}/\text{rGO}$ -1, (c,d) $\text{Ni}(\text{OH})_2/\text{Ni}/\text{rGO}$ -2, (e,f) $\text{Ni}(\text{OH})_2/\text{Ni}/\text{rGO}$ -3, (g) $\text{Ni}(\text{OH})_2/\text{Ni}/\text{rGO}$ -4, and (h) $\text{Ni}(\text{OH})_2/\text{Ni}/\text{rGO}$ -5 composite catalysts. The images of (b,d,f) are high-magnification areas indicated by the yellow arrows in (a,c,e).

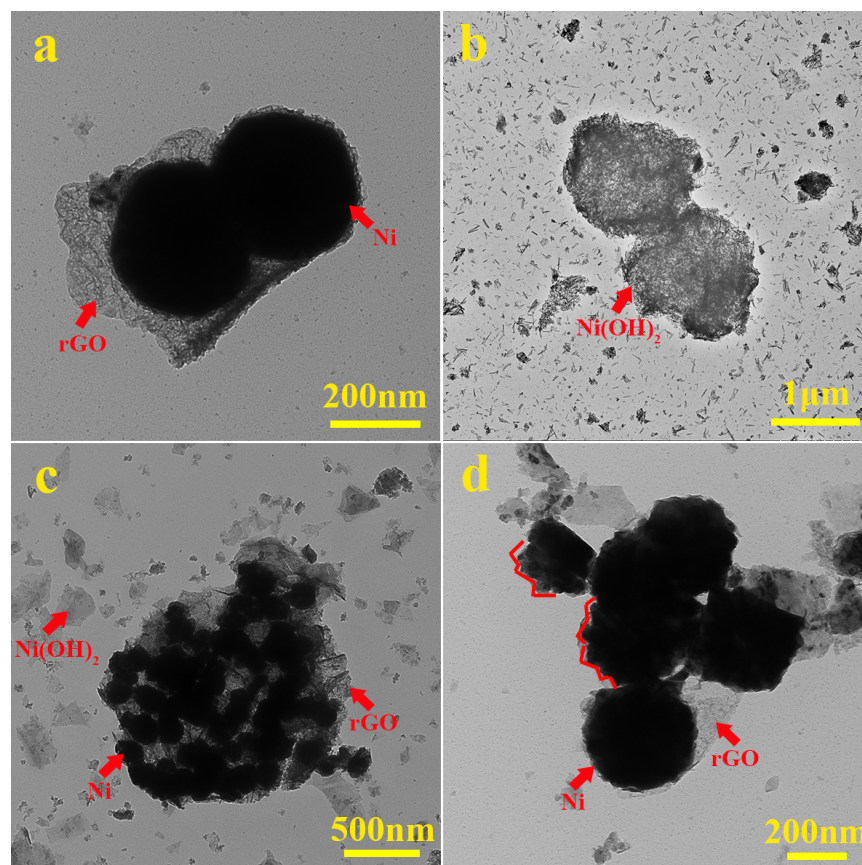


Figure 2. TEM images of (a) Ni/rGO, (b) Ni(OH)₂/Ni/rGO-1, (c) Ni(OH)₂/Ni/rGO-3, and (d) Ni(OH)₂/Ni/rGO-5 catalysts, respectively.

2.2. Microstructure Analysis

A series of characterizations, including XRD and XPS analysis, were performed to identify the component of the Ni(OH)₂/Ni/rGO hybrid. The XRD patterns of Ni/rGO, Ni(OH)₂/Ni/rGO-1, Ni(OH)₂/Ni/rGO-3, and Ni(OH)₂/Ni/rGO-5 catalysts are displayed in Figure 3a. The 4 peaks at 44.92, 52.26, 76.72, and 93.24° arise from Ni (JCPDS No. 65-2865), which conform to the (111), (200), (220), and (311) lattice planes, respectively. It is observed that the preferential orientation of the Ni/rGO, Ni(OH)₂/Ni/rGO-1, Ni(OH)₂/Ni/rGO-3, and Ni(OH)₂/Ni/rGO-5 composite catalysts are the (111) crystal plane. According to the illustration of reported papers [31,32], the Ni(111) plane has a more advantageous effect on enhancing the electrocatalytic performance of HER than other planes. In addition, Ni/rGO and Ni(OH)₂/Ni/rGO-5 catalysts show a stronger peak intensity of Ni than those of Ni(OH)₂/Ni/rGO-1 and Ni(OH)₂/Ni/rGO-3 catalysts, which is due to a layer of Ni(OH)₂ nanosheets covering the surface of Ni particles of Ni(OH)₂/Ni/rGO-1 and Ni(OH)₂/Ni/rGO-3 catalysts, so that the peak strength of Ni is weakened. It is worth noting that the diffraction peaks located at 33.62, 38.98, and 52.26° correspond to the (100), (101), and (102) planes of β-Ni(OH)₂ (JCPDS No. 14-0117), which are only reflected on the Ni(OH)₂/Ni/rGO-1 pattern. As displayed in Figure 3b, there are no characteristic diffraction peaks of Ni(OH)₂ in the samples of Ni(OH)₂/Ni/rGO-3 and Ni(OH)₂/Ni/rGO-5 catalysts. This is because the Ni(OH)₂ nanosheets gradually disappear and dissolve in the solution as the concentration of urea increases. XRD analysis indicates that Ni(OH)₂ successfully forms on the Ni surface and falls off as the urea concentration increases. Such observations are in keeping with the analysis results of SEM and TEM. Meanwhile, we did not find the characteristics of rGO diffraction peaks in the XRD pattern of Ni(OH)₂/Ni/rGO coatings. This is due to the diffraction intensity of Ni being too strong, thus weakening the diffraction intensity of rGO.

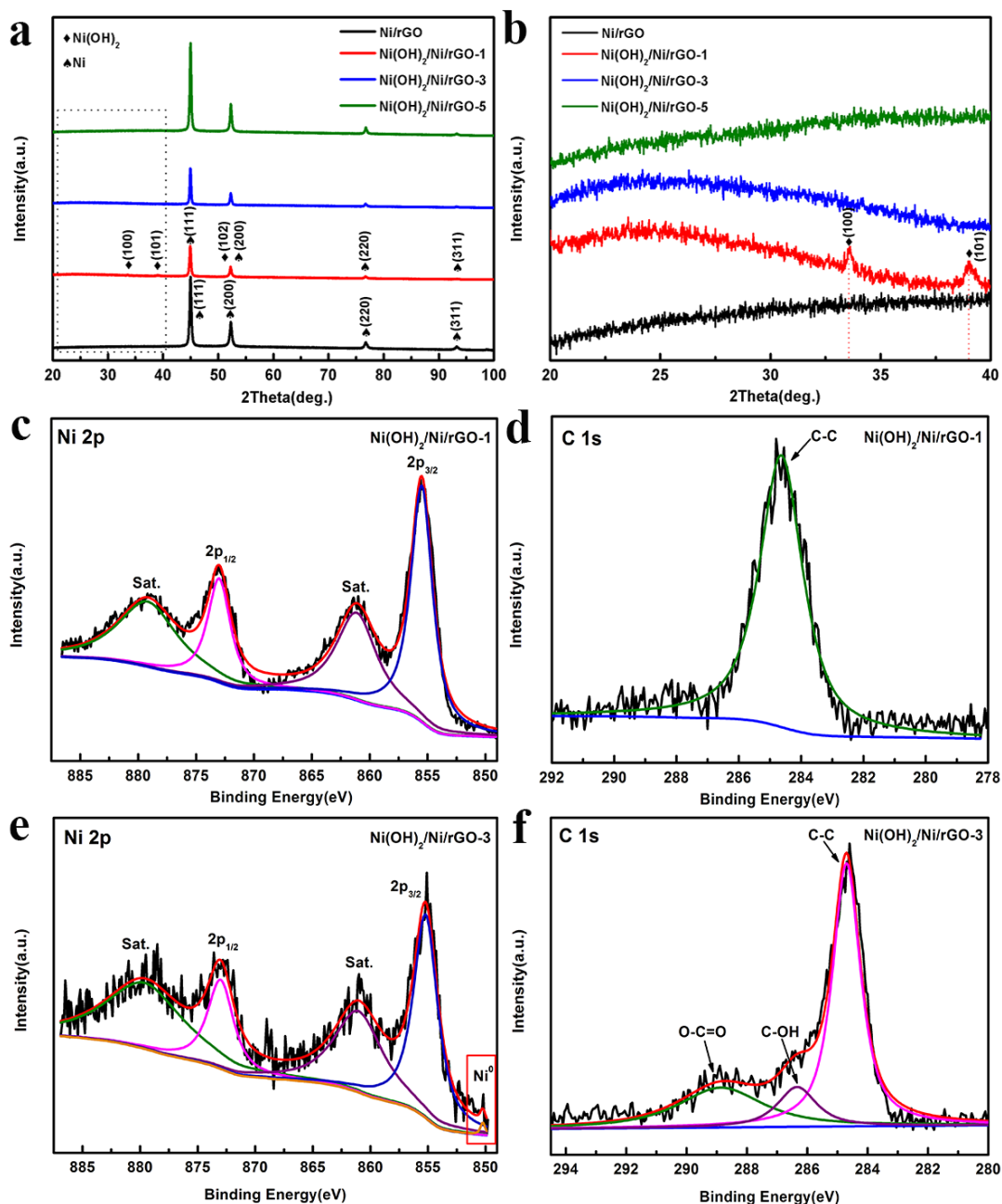


Figure 3. XRD patterns of (a) Ni/rGO, Ni(OH)₂/Ni/rGO-1, Ni(OH)₂/Ni/rGO-3, and Ni(OH)₂/Ni/rGO-5 composite catalysts; (b) is the enlarged rectangle region of (a). XPS spectra of (c) Ni 2p and (d) C 1s of Ni(OH)₂/Ni/rGO-1 catalyst. XPS spectra of (e) Ni 2p and (f) C 1s of Ni(OH)₂/Ni/rGO-3 catalyst.

XPS testing was further carried out to research the surface chemical composition of the Ni(OH)₂/Ni/rGO hybrid catalysts. The survey XPS spectra in Figures S7a and S8a verify the coexistence of Ni, C, and O elements on the material surface of Ni(OH)₂/Ni/rGO-1 and Ni(OH)₂/Ni/rGO-3 catalysts. The high-resolution XPS spectrum of the Ni(OH)₂/Ni/rGO-1 material for the Ni region, as shown in Figure 3c, indicates that the peaks at 855.5 and 873.0 eV accord with the Ni 2p_{3/2} levels, and signals at 873.0 and 879.2 eV conform to Ni 2p_{1/2} levels. The C element of the Ni(OH)₂/Ni/rGO-1 sample is presented in Figure 3d. The main peak at 284.6 eV is from the C–C coordination in the rGO. It is different from the Ni(OH)₂/Ni/rGO-1 sample. The high-resolution Ni 2p spectrum of Ni(OH)₂/Ni/rGO-3 sample reflects an extra peak at 850.2 eV (Figure 3e), which arises from Ni⁰ from the Ni/rGO

catalyst. Once again, this implies that Ni(OH)₂ nanosheets gradually disappear as the concentration of urea increases. The high-resolution C 1s spectrum of the Ni(OH)₂/Ni/rGO-3 sample exists in three states, as shown in Figure 3f. The peaks at 284.7, 286.3, and 288.9 eV belong to the bonds of C–C, C–OH, and O–C=O, respectively. As presented in Figures S7b and S8b, the O 1s spectrum of both the Ni(OH)₂/Ni/rGO-1 and Ni(OH)₂/Ni/rGO-3 catalysts contributes two forms of oxygen, which are represented as O1 and O2. The signal O1 located at ~531.4 eV is attributed to a higher number of hydroxide species and adsorbed oxygen at the surface of the hybrid catalyst. The signal O2 located at ~530.8 eV generally ascribes oxygen atoms at the surface of hydroxyl groups. In addition, the intensity of the O 1s signal is sufficiently strong, which reflects the formation of Ni(OH)₂ or is apparently oxidized at the surface of the material.

2.3. Electrochemical Activity and Stability

Figure 4 summarizes the electrocatalytic performance of HER (2H₂O + 2e[−] → H₂ + 2OH[−], HER in alkaline solution) of the Ni(OH)₂/Ni/rGO composite catalysts. The LSV plots of the Ni/rGO, Ni(OH)₂/Ni/rGO-1, Ni(OH)₂/Ni/rGO-2, Ni(OH)₂/Ni/rGO-3, Ni(OH)₂/Ni/rGO-4, Ni(OH)₂/Ni/rGO-5, and Pt/C cathodes after iR-correction are presented in Figure 4a. As shown in Table 1, it is apparent that the Ni(OH)₂/Ni/rGO-3 cathode presents better catalytic activity among these catalysts, which demands overpotentials of 161.7 and 41.00 mV to acquire current densities of 100 and 10 mA cm^{−2}, respectively. Moreover, the Ni/rGO, Ni(OH)₂/Ni/rGO-1, Ni(OH)₂/Ni/rGO-2, and Ni(OH)₂/Ni/rGO-4, Ni(OH)₂/Ni/rGO-5 catalysts demand overpotentials of 196.0 and 62.01 mV, 183.5 and 64.69 mV, 176.8 and 68.67 mV, 171.6 and 51.00 mV, and 200.5 and 91.38 mV to acquire current densities of 100 and 10 mA cm^{−2}, respectively. And the obtained Pt/C catalyst demands overpotentials of 97 and 27 mV to acquire current densities of 100 and 10 mA cm^{−2}. The HER performance of the Ni(OH)₂/Ni/rGO-3 composite catalyst is closest to the Pt/C cathode. Remarkably, compared to other similar Ni-based catalysts, the Ni(OH)₂/Ni/rGO-3 hybrid synthesized in this paper exhibits much better catalytic activity on HER than other catalysts of reported papers, as displayed in Table S1. Ni(OH)₂/Ni/rGO-3 shows lower overpotential than those of NiFe LDH-NS [25], FNHNs/NF [26], Ni(OH)₂/NF [27], NiP₂/NiSe₂ [28], NiCo₂S₄ NA/CC [33], NiS/Ni foam [34], Ni₂P [35], and NiMo HNRs/TiM [36].

Table 1. Electrochemical parameters on HER recorded in 1 M KOH solution at 298 K.

Composite Electrodes	b (mV dec ^{−1})	j ₀ (mA cm ^{−2})	R _s (Ω cm ^{−2})	R _{ct} (Ω cm ^{−2})	η ₁₀₀ (mV)	η ₁₀ (mV)
Ni/rGO	126.4	2.605	0.3835	4.064	196.0	62.01
Ni(OH) ₂ /Ni/rGO-1	108.8	2.039	0.9214	3.799	183.5	64.69
Ni(OH) ₂ /Ni/rGO-2	121.1	2.703	0.7225	2.993	176.8	68.67
Ni(OH) ₂ /Ni/rGO-3	79.45	3.018	0.6030	2.106	161.7	41.00
Ni(OH) ₂ /Ni/rGO-4	79.65	2.149	0.6797	2.570	171.6	51.00
Ni(OH) ₂ /Ni/rGO-5	140.1	2.226	0.6584	5.632	200.5	91.38

Currently, the Tafel curves and exchange current density (j₀) were extensively applied to research the HER mechanism of the Ni(OH)₂/Ni/rGO cathodes. As displayed in Figure 4b, the Ni(OH)₂/Ni/rGO-3 cathode exhibits a Tafel slope of 79.45 mV dec^{−1} in the alkaline solution, which is much lower than those of Ni/rGO (126.4 mV dec^{−1}), Ni(OH)₂/Ni/rGO-1 (108.8 mV dec^{−1}), Ni(OH)₂/Ni/rGO-2 (121.1 mV dec^{−1}), Ni(OH)₂/Ni/rGO-4 (79.65 mV dec^{−1}), and Ni(OH)₂/Ni/rGO-5 (140.1 mV dec^{−1}) catalysts, indicating that all Ni(OH)₂/Ni/rGO cathodes are in accordance with the Volmer–Heyrovsky mechanism on HER. It is worth noting that the Pt/C cathode exhibits a Tafel slope of only 40 mV dec^{−1} closest to Ni(OH)₂/Ni/rGO-3 cathode. The j₀ is also identified as significant data for the electrochemical catalysis mechanism, and this reflects the difficulty of the electron transport rate of the composite catalyst on HER. According to the known formula $\eta = \text{blog}(j/j_0)$ [37], where j is the current density, j₀ is the exchange current density, and b is the Tafel slope, we can get j₀ values. As revealed in Table 1, the obtained j₀ value of

the Ni(OH)₂/Ni/rGO-3 catalyst is 3.018 mA cm⁻², which is much higher than those of the Ni/rGO (2.605 mA cm⁻²), Ni(OH)₂/Ni/rGO-1 (2.039 mA cm⁻²), Ni(OH)₂/Ni/rGO-2 (2.703 mA cm⁻²), Ni(OH)₂/Ni/rGO-4 (2.149 mA cm⁻²), and Ni(OH)₂/Ni/rGO-5 (2.149 mA cm⁻²) composite catalysts, suggesting that the Ni(OH)₂/Ni/rGO-3 cathode demands a lower driving power to enhance the hydrogen evolution activity.

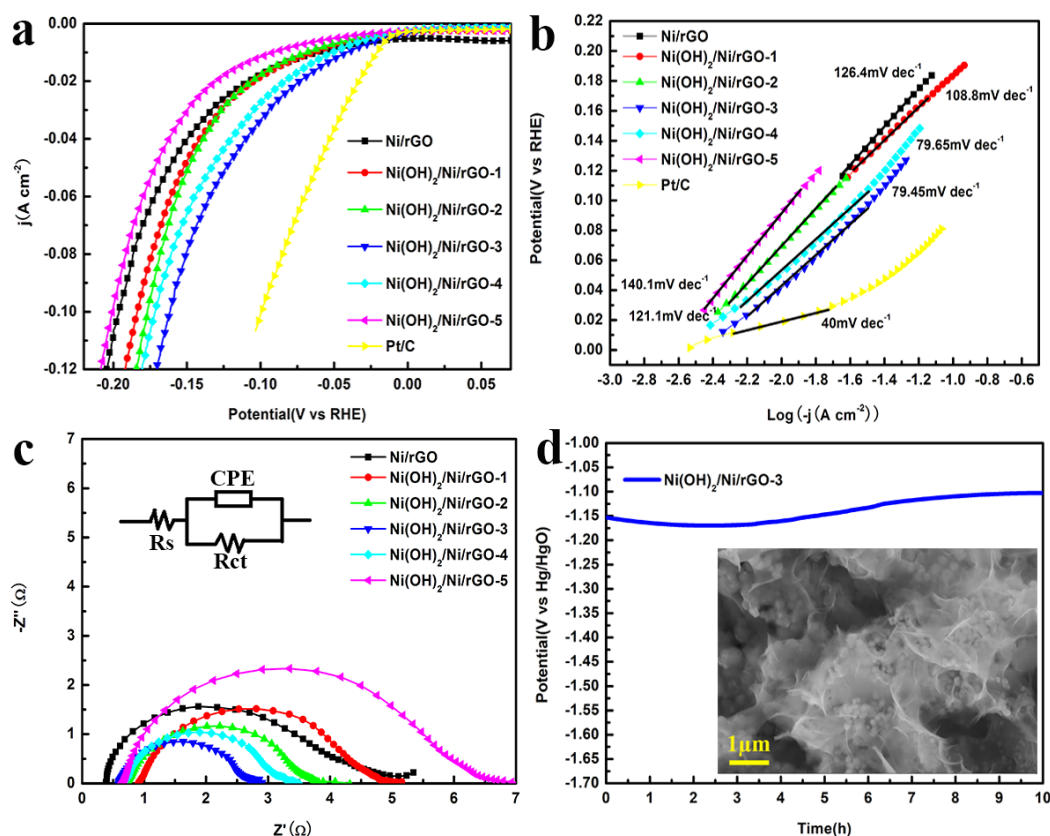


Figure 4. (a) LSV curves and (b) Tafel plots of Ni/rGO, Ni(OH)₂/Ni/rGO-1, Ni(OH)₂/Ni/rGO-2, Ni(OH)₂/Ni/rGO-3, Ni(OH)₂/Ni/rGO-4, Ni(OH)₂/Ni/rGO-5, and Pt/C catalysts. (c) EIS spectra of Ni/rGO, Ni(OH)₂/Ni/rGO-1, Ni(OH)₂/Ni/rGO-2, Ni(OH)₂/Ni/rGO-3, Ni(OH)₂/Ni/rGO-4, and Ni(OH)₂/Ni/rGO-5 composite catalysts. The inset in (c) is an equivalent electrical circuit used to model the HER kinetics process. (d) Chronopotentiometry test of Ni(OH)₂/Ni/rGO-3 catalyst at the current density of 100 mA cm⁻² for 10 h. The inset in (d) is an SEM image of the Ni(OH)₂/Ni/rGO-3 catalyst after long-term electrolysis.

EIS testing was then operated to gain more information on the electrocatalytic property of composite catalysts in the case of a cathode overpotential of 125 mV on HER. The corresponding Nyquist curves are revealed in Figure 4c, and the curves were characterized by a model with the single-adsorbate mechanism [38], as shown in the inset of Figure 4c. As presented in Table 1, the R_{ct} of the Ni/rGO, Ni(OH)₂/Ni/rGO-1, Ni(OH)₂/Ni/rGO-2, Ni(OH)₂/Ni/rGO-3, Ni(OH)₂/Ni/rGO-4, and Ni(OH)₂/Ni/rGO-5 catalysts are 4.064, 3.799, 2.993, 2.106, 2.570, and 5.632 Ω cm⁻², respectively. The above results are consistent with the LSV and Tafel analysis assessment, and it further indicates that the Ni(OH)₂/Ni/rGO-3 catalyst shows higher electrocatalytic activity and good electrical conductivity.

Chronopotentiometry measurement is currently aimed at assessing the durability and stability of electrocatalysts on HER. It is worth noting that the Ni(OH)₂/Ni/rGO-3 cathode was measured at the current density of 100 mA cm⁻¹ for 10 h. As presented in Figure 4d, the chronopotentiometric curve states that the Ni(OH)₂/Ni/rGO-3 cathode almost keeps a constant potential around 1.10–1.15 V. In addition, the SEM image after

chronopotentiometry testing of Ni(OH)₂/Ni/rGO-3 cathode is also displayed in Figure 4d. Obviously, after 10 h of chronopotentiometric testing, its morphology did not change visibly as shown in the SEM image. Thus, the result of chronopotentiometry analysis illustrates the good durability and stability of the Ni(OH)₂/Ni/rGO-3 catalyst. Also, the LSV curves of the Ni(OH)₂/Ni/rGO-3 sample before and after stability analysis (Figure S9) display negligible change.

Electrocatalytic properties of different electrocatalysts for OER were studied in a classical three-electrode configuration ($4\text{OH}^- \rightarrow \text{O}_2 + 2\text{H}_2\text{O} + 4\text{e}^-$, OER in alkaline solution). As displayed in Figure 5a, the Ni(OH)₂/Ni/rGO-1 sample presents outstanding performance for OER with a low overpotential. Nevertheless, RuO₂ shows poor performance for OER. In this process, the overpotentials needed to reach 50 and 100 mA cm⁻² for Ni/rGO, Ni(OH)₂/Ni/rGO-1, Ni(OH)₂/Ni/rGO-3, and Ni(OH)₂/Ni/rGO-5 are 397 and 472 mV, 331 and 407 mV, 389 and 440 mV, 403 and 465 mV, respectively. Similarly, Ni(OH)₂/Ni/rGO-1 presents superior OER activity than other reported papers [25,26,28,34–36], as shown in Table S1. In addition, the long-term stability of this efficient oxygen evolution anode was measured. A chronopotentiometry test of the Ni(OH)₂/Ni/rGO-1 catalyst at the current density of 100 mA cm⁻² for 10 h was applied without obvious decay (Figure 5b) and the appearance of the Ni(OH)₂/Ni/rGO-1 catalyst did not change (inset in Figure 5b). The good electrochemical property of the Ni(OH)₂/Ni/rGO-1 catalyst on OER is mainly because Ni(OH)₂ nanosheets help accelerate the cracking of water molecules. The LSV curves of the Ni(OH)₂/Ni/rGO-1 sample before and after stability analysis (Figure S10) display a tiny change. The overpotentials needed to reach 50 and 100 mA cm⁻² for Ni(OH)₂/Ni/rGO-1 after the chronopotentiometry test are 366 and 420 mV.

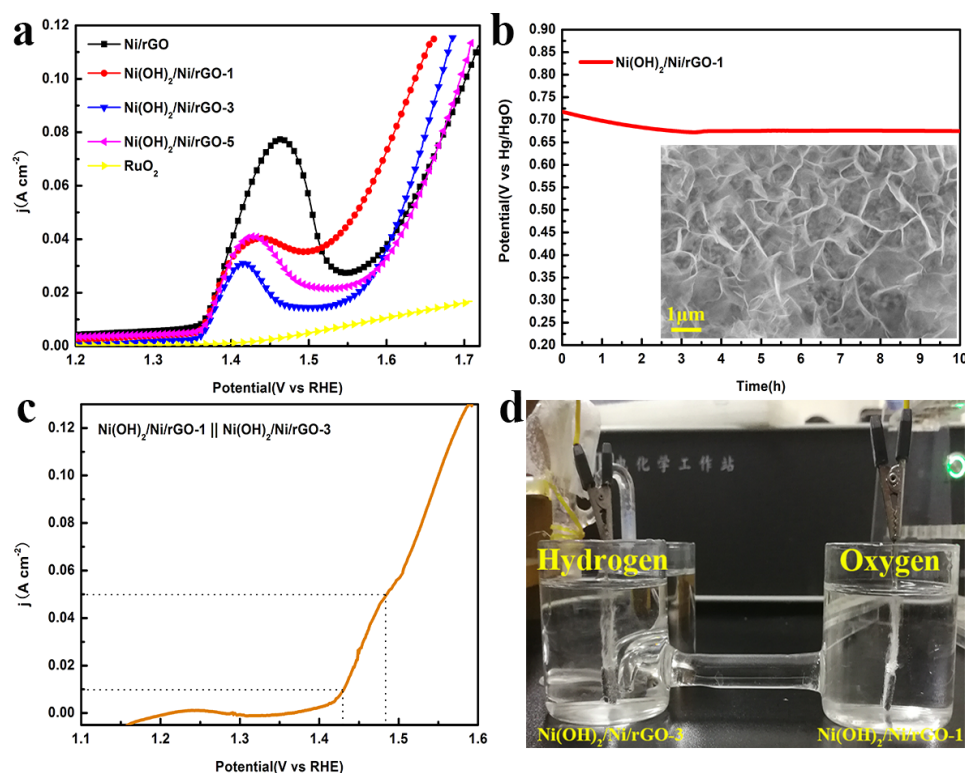


Figure 5. (a) LSV curves for Ni/rGO, Ni(OH)₂/Ni/rGO-1, Ni(OH)₂/Ni/rGO-3, Ni(OH)₂/Ni/rGO-5, and RuO₂ catalysts without iR correction at a sweep rate of 5 mV s⁻¹. (b) Chronopotentiometry test of Ni(OH)₂/Ni/rGO-1 catalyst at the current density of 100 mA cm⁻² for 10 h. The inset in (b) is an SEM image of the Ni(OH)₂/Ni/rGO-1 catalyst after long-term electrolysis. (c) LSV plot of overall water splitting by using Ni(OH)₂/Ni/rGO-1 as an anode and Ni(OH)₂/Ni/rGO-3 as a cathode. (d) The real image of a two-electrode electrolyzer system with Ni(OH)₂/Ni/rGO-1 as an anode and Ni(OH)₂/Ni/rGO-3 as a cathode with gas evolution.

Finally, the Ni(OH)₂/Ni/rGO-3 and Ni(OH)₂/Ni/rGO-1 catalysts were used as HER and OER catalysts for water splitting in 1 M KOH. Figure 5c presents the LSV curve of overall water splitting, and it reaches 1.43 and 1.48 V at 10 and 50 mA cm⁻², respectively, which is much lower than some reported Ni-based catalysts [26–28,33–36], as shown in Table S1. Figure 5d shows a real overall water-splitting system in 1 M KOH solution. There produced many bubbles on the cathode and anode surfaces in succession. All of the experiments described above reveal that the Ni(OH)₂/Ni/rGO catalyst is a highly effective bifunctional catalyst in strong alkaline electrolytes.

Based on a series of experimental results, this outstanding catalytic performance of the Ni(OH)₂/Ni/rGO catalyst for HER, OER, and water splitting can be attributed to several features: (1) the Ni(OH)₂/Ni/rGO catalyst has unique bifunctional metal-metal hydroxide system, which facilitates different parts of the overall multistep process in an alkaline environment. Ni(OH)₂ nanosheets offer the active sites for splitting water, and metal Ni accelerate adsorption of the H_{ads} and its following association to form H₂ from these intermediates; (2) the rGO layer has very good electrical conductivity; meanwhile, the rGO sheets have positive effects on increasing the surface roughness of electrode and refining the Ni particles, thereby promoting the specific surface area of the composite catalyst and enhancing its electrochemical activity; the large surface area of Ni(OH)₂/Ni/rGO catalyst gives it countless active sites; and (3) the superior property of Ni(OH)₂/Ni/rGO catalyst comes from its unique tertiary structure. Taking advantage of the catalytic characteristics of rGO, Ni, and Ni hydroxide is to design a new-style and environment-friendly catalyst. These advantages might encourage the design and development of new low-cost and high-efficiency electrodes for water electrolysis.

3. Experiment

3.1. Preparation of Ni/rGO Composite Catalyst

The growth method and characterization analysis of Ni/rGO composite catalyst were introduced in the supporting information and our reported paper [30].

3.2. Preparation of Ni(OH)₂/Ni/rGO Composite Catalyst

The Ni(OH)₂/Ni/rGO composite catalysts were manufactured by a simple hydrothermal method. In a classic way, 50 mL of deionized water dissolved 0.1, 0.5, 1.0, 1.5, and 2.0 g of urea, with the urea concentrations being 2, 10, 20, 30, and 40 mg mL⁻¹, respectively. After uniformly stirring, the end solution was transferred to a Teflon-sealed autoclave and the Ni/rGO coating (4 cm × 2 cm) was vertically placed into the above solution and reacted at 160 °C for 5 h to synthesize the Ni(OH)₂/Ni/rGO composite cathodes. After cooling to room temperature, the product was washed with deionized water and ethanol for a few cycles, and it was ultimately dried at 60 °C. The above five composite cathodes were, respectively, named Ni(OH)₂/Ni/rGO-1, Ni(OH)₂/Ni/rGO-2, Ni(OH)₂/Ni/rGO-3, Ni(OH)₂/Ni/rGO-4, and Ni(OH)₂/Ni/rGO-5.

3.3. Characterization

The microstructures of the obtained catalysts were studied by X-ray photoelectron spectroscopy (XPS, Manchester, England) with a Kratos XSAM-800 spectrometer and X-ray diffraction (XRD, RigakuD/MAX 2500/PC, Japan) with Cu K α radiation ($\lambda = 1.5418 \text{ \AA}$). The morphologies of the obtained catalysts were studied by transmission electron microscopy (TEM, JEM 2100F, Japan Electronics Co., LTD., Tokyo, Japan) executed at 100 kV, atomic force microscopy (AFM, Bruker Multimode 8, Germany), and scanning electron microscopy (SEM, Carl Zeiss Super55, Carl Zeiss NTS GmbH, Oberkochen, Germany) with an accelerating voltage of 20 kV. The chemical composition analysis of the hybrid catalyst was conducted by applying an energy dispersive spectrometer (EDS) linked to the SEM instrument.

3.4. Electrochemical Measurements

All the tests were measured in a three-electrode electrochemical cell at 25 °C, and all the electrocatalytic performance measurements were performed using a CHI 660E electrochemical apparatus (CH Instruments, Inc., Shanghai, China). A Pt plate of 1 cm × 1 cm × 0.1 mm was used as the counter electrode, an Hg/HgO electrode in 1 M KOH was used as the reference electrode and the obtained Ni(OH)₂/Ni/rGO composite coating of 1 cm × 1 cm was used as the working electrode. Generally, 30 mg 20 wt% Pt/C and RuO₂ were dispersed in a 10 mL mixed solution of 5 mL distilled water and 5 mL ethanol with 100 μL Nafion solution, respectively, followed by 2 h ultrasonic treatment to get the uniform ink. The commercial Pt/C cathode and RuO₂ anode were fabricated by dripping the above hybrid ink onto a Ni foam sheet with 1 cm × 1 cm and, afterward, drying at 25 °C for 10 h. The linear sweep voltammetry (LSV) curves were conducted at a scan rate of 5 mV s⁻¹. The Tafel curves were derived from the transformation of LSV tests. Furthermore, the electrochemical impedance spectroscopy (EIS) was carried out at a potential of -1.05 V vs. Hg/HgO ($\eta = 125$ mV), at a frequency from 100 kHz to 0.01 Hz with an AC amplitude of 5 mV. The stability measurements were performed at 100 mA cm⁻² for 10 h each.

4. Conclusions

In summary, we report a successful method of a series of Ni(OH)₂/Ni/rGO hybrid catalysts on Ni foam in an economical and simple way. We combine the catalytic characteristics of Ni and Ni(OH)₂ by creating a new bifunctional metal-metal hydroxide system. The prepared composite electrode has a unique hierarchical structure, large specific surface area, and excellent and stable HER and OER performances. The obtained Ni(OH)₂/Ni/rGO-3 catalyst displays outstanding performance with small overpotentials of 161.7 and 41 mV to acquire current densities of 100 and 10 mA cm⁻² on HER. Ni(OH)₂/Ni/rGO-1 catalyst requires 331 and 407 mV overpotentials to afford 50 and 100 mA cm⁻² on OER. Moreover, both catalysts need 10 mA·cm⁻² at a cell voltage of 1.43 V for water splitting in an alkaline solution. This study can provide a fresh perspective on non-precious metals as bifunctional electrocatalysts.

Supplementary Materials: The following supporting information can be downloaded at <https://www.mdpi.com/article/10.3390/catal14050309/s1>, Preparation of Ni/rGO composite catalyst. Figure S1. Low-magnification SEM images of Ni foam; Figure S2. High-magnification SEM image of Ni/rGO composite catalyst; Figure S3. Low-magnification SEM images of Ni(OH)₂/Ni/rGO-1 composite catalyst; Figure S4. AFM image of Ni(OH)₂ nanosheets spalled off Ni(OH)₂/Ni/rGO-1 catalyst (with 1 h sonication), and inset image is corresponding AFM height image; Figure S5. (a–c) Elemental mapping of individual elements (C, O, Ni) of image Figure 1a. (d) EDS analysis of Ni(OH)₂/Ni/rGO-1 composite coating; Figure S6. The digital photos of the color of the urea solution after hydrothermal process. The color of the urea solution changes obviously from colorless to dark blue. (a) Ni(OH)₂/Ni/rGO-1, (b) Ni(OH)₂/Ni/rGO-2, (c) Ni(OH)₂/Ni/rGO-3, (d) Ni(OH)₂/Ni/rGO-4, and (e) Ni(OH)₂/Ni/rGO-5 composite catalysts; Figure S7. (a) XPS survey spectrum for Ni(OH)₂/Ni/rGO-1. (b) XPS spectrum of O 1s of Ni(OH)₂/Ni/rGO-1 catalyst; Figure S8. (a) XPS survey spectrum for Ni(OH)₂/Ni/rGO-3. (b) XPS spectrum of O 1s of Ni(OH)₂/Ni/rGO-3 catalyst; Figure S9. LSV curves for Ni(OH)₂/Ni/rGO-3 before and after chronopotentiometry test; Figure S10. LSV curves for Ni(OH)₂/Ni/rGO-1 before and after chronopotentiometry test; Table S1. Comparison of electrocatalytic activity for HER, OER and EWS of diverse Ni-based catalysts in alkaline solution. References [25–30,33–36] are cited in the Supplementary Materials.

Author Contributions: Conceptualization, A.S. and X.Q.; methodology, L.W.; validation, L.W.; formal analysis, Y.L. and M.D.; investigation, L.W.; data curation, L.W.; writing—original draft preparation, L.W.; writing—review and editing, A.S.; resources, Z.M. and G.S.; supervision, X.Q. All authors have read and agreed to the published version of the manuscript.

Funding: This work was financially supported by the Doctoral Scientific Research Foundation of Shijiazhuang University (20BS001), the Science and Technology Research Project of Colleges and Univer-

sities in Hebei Province (Z2020127), and the National Natural Science Foundation of China (52074241, 52174281, 51674221 and 51704261), the Natural Science Foundation of Hebei Province (B2021203016 and E2023203209), the Science Research Project of Hebei Education Department (BJ2020038) and Cultivation Project for Basic Research and Innovation of Yanshan University (2021LGDZ013), the Hebei Provincial Department of Human Resources and Social Security (C20230328).

Data Availability Statement: The data that support the findings of this study are available from the corresponding author upon reasonable request.

Conflicts of Interest: The authors declare no conflicts of interest.

References

1. Tian, H.; Song, A.; Zhang, P.; Sun, K.; Wang, J.; Sun, B.; Fan, Q.; Shao, G.; Chen, C.; Liu, H.; et al. High durability of Fe-N-C single-atom catalysts with carbon vacancies toward the oxygen reduction reaction in alkaline media. *Adv. Mater.* **2023**, *35*, 2210714. [[CrossRef](#)] [[PubMed](#)]
2. Song, A.; Song, S.; Duanmu, M.; Tian, H.; Liu, H.; Qin, X.; Shao, G.; Wang, G. Recent progress of non-noble metallic heterostructures for the electrocatalytic hydrogen evolution. *Small Sci.* **2023**, *3*, 2300036. [[CrossRef](#)]
3. Tian, H.; Song, A.; Tian, H.; Liu, J.; Shao, G.; Liu, H.; Wang, G. Single-atom catalysts for high-energy rechargeable batteries. *Chem. Sci.* **2021**, *12*, 7656–7676. [[CrossRef](#)] [[PubMed](#)]
4. Cao, X.; Huo, J.; Li, L.; Qu, J.; Zhao, Y.; Chen, W.; Liu, C.; Liu, H.; Wang, G. Recent advances in engineered Ru-based electrocatalysts for the hydrogen/oxygen conversion reactions. *Adv. Energy Mater.* **2022**, *12*, 2202119. [[CrossRef](#)]
5. Huo, J.; Cao, X.; Tian, Y.; Li, L.; Qu, J.; Xie, Y.; Nie, X.; Zhao, Y.; Zhang, J.; Liu, H. Atomically dispersed Mn atoms coordinated with N and O within an N-doped porous carbon framework for boosted oxygen reduction catalysis. *Nanoscale* **2023**, *15*, 5448–5457. [[CrossRef](#)]
6. Huo, J.; Shen, Z.; Cao, X.; Li, L.; Zhao, Y.; Liu, H.; Wang, G. Macro/micro-environment regulating carbon-supported single-atom catalysts for hydrogen/oxygen conversion reactions. *Small* **2022**, *18*, 2202394. [[CrossRef](#)] [[PubMed](#)]
7. Xiao, Z.; Zhang, C.; Li, P.; Wang, D.; Zhang, X.; Wang, L.; Zou, J.; Li, G. Engineering oxygen vacancies on Tb-doped ceria supported Pt catalyst for hydrogen production through steam reforming of long-chain hydrocarbon fuels. *Chin. J. Chem. Eng.* **2024**, *68*, 181–192. [[CrossRef](#)]
8. Bao, W.; Tang, Y.; Yu, J.; Yan, W.; Wang, C.; Li, Y.; Wang, Z.; Yang, J.; Zhang, L.; Yu, F. Si-doped ZnAl-LDH nanosheets by layer-engineering for efficient photoelectrocatalytic water splitting. *Appl. Catal. B Environ. Energy* **2024**, *346*, 123706. [[CrossRef](#)]
9. Chen, F.; Liu, H.; Yang, F.; Che, S.; Chen, N.; Xu, C.; Wu, N.; Sun, Y.; Yu, C.; Li, Y. Multifunctional electrocatalyst based on MoCoFe LDH nanoarrays for the coupling of high efficiency electro-fenton and water splitting process. *Chem. Eng. J.* **2023**, *467*, 143274. [[CrossRef](#)]
10. Sun, H.; Song, S.; Xu, X.; Dai, J.; Yu, J.; Zhou, W.; Shao, Z.; Jung, W. Recent progress on structurally ordered materials for electrocatalysis. *Adv. Energy Mater.* **2021**, *11*, 2101937. [[CrossRef](#)]
11. Fan, X.; Li, B.; Zhu, C.; Yan, F.; Zhang, X.; Chen, Y. Nitrogen and sulfur Co-doped carbon-coated Ni₃S₂/MoO₂ nanowires as bifunctional catalysts for alkaline seawater electrolysis. *Small* **2024**, 2309655. [[CrossRef](#)]
12. Zhao, Z.; Li, Z.; Zhang, Z.; Meng, X. Fe/P dual-doping NiMoO₄ with hollow structure for efficient hydrazine oxidation-assisted hydrogen generation in alkaline seawater. *Appl. Catal. B Environ. Energy* **2024**, *347*, 123805. [[CrossRef](#)]
13. Ding, X.; Xiang, J.; Wan, Y.; Song, F. Elemental charge engineering in cobalt and cobalt-phosphide interface for enhanced oxygen evolution and urea oxidation reactions. *ACS Appl. Energy Mater.* **2024**, *9*, 695–701. [[CrossRef](#)]
14. Kulkarni, R.; Lingamdinne, L.P.; Karri, R.R.; Momin, Z.H.; Koduru, J.R.; Chang, Y.Y. Catalytic efficiency of LDH@ carbonaceous hybrid nanocomposites towards water splitting mechanism: Impact of plasma and its significance on HER and OER activity. *Coord. Chem. Rev.* **2023**, *497*, 215460. [[CrossRef](#)]
15. Ren, J.T.; Chen, L.; Tian, W.W.; Song, X.L.; Kong, Q.H.; Wang, H.Y.; Yuan, Z.Y. Rational synthesis of core-shell-structured nickel sulfide-based nanostructures for efficient seawater electrolysis. *Small* **2023**, *19*, 2300194. [[CrossRef](#)]
16. Shankar Naik, S.; Theerthagiri, J.; Nogueira, F.S.; Lee, S.J.; Min, A.; Kim, G.A.; Maia, G.; Pinto, L.M.C.; Choi, M.Y. Dual-cation-coordinated CoFe-layered double-hydroxide nanosheets using the pulsed laser ablation technique for efficient electrochemical water splitting: Mechanistic screening by in situ/operando Raman and density functional theory calculations. *ACS Catalysis* **2023**, *13*, 1477–1491. [[CrossRef](#)]
17. Chen, M.; Abazari, R.; Sanati, S.; Chen, J.; Sun, M.; Bai, C.; Kirillov, A.M.; Zhou, Y.; Hu, G. Compositional engineering of HKUST-1/sulfidized NiMn-LDH on functionalized MWCNTs as remarkable bifunctional electrocatalysts for water splitting. *Carbon Energy* **2023**, *5*, e459. [[CrossRef](#)]
18. Hu, Y.; Shen, T.; Song, Z.; Wu, Z.; Bai, S.; Liu, G.; Sun, X.; Wang, Y.; Hu, S.; Zheng, L.; et al. Atomic modulation of single dispersed Ir species on self-supported NiFe layered double hydroxides for efficient electrocatalytic overall water splitting. *ACS Catalysis* **2023**, *13*, 11195–11203. [[CrossRef](#)]
19. Huo, J.M.; Ma, Z.L.; Wang, Y.; Cao, Y.J.; Jiang, Y.C.; Li, S.N.; Chen, Y.; Hu, M.C.; Zhai, Q.G. Monodispersed Pt sites supported on NiFe-LDH from synchronous anchoring and reduction for high efficiency overall water splitting. *Small* **2023**, *19*, 2207044. [[CrossRef](#)]

20. Tan, L.; Wang, H.; Qi, C.; Peng, X.; Pan, X.; Wu, X.; Wang, Z.; Ye, L.; Xiao, Q.; Luo, W.; et al. Regulating Pt electronic properties on NiFe layered double hydroxide interface for highly efficient alkaline water splitting. *Appl. Catal. B Environ.* **2024**, *342*, 123352. [[CrossRef](#)]
21. Gao, M.; Sheng, W.; Zhuang, Z.; Fang, Q.; Gu, S.; Jiang, J.; Yan, Y. Efficient water oxidation using nanostructured α -nickel-hydroxide as an electrocatalyst. *J. Am. Chem. Soc.* **2014**, *136*, 7077–7084. [[CrossRef](#)]
22. Li, X.; Han, G.Q.; Liu, Y.R.; Dong, B.; Hu, W.H.; Shang, X.; Chai, Y.M.; Liu, C.G. NiSe@NiOOH core-shell hyacinth-like nanostructures on nickel foam synthesized by in situ electrochemical oxidation as an efficient electrocatalyst for the oxygen evolution reaction. *ACS Appl. Mater. Interfaces* **2016**, *8*, 20057–20066. [[CrossRef](#)]
23. Li, R.; Xu, H.; Yang, P.; Wang, D.; Li, Y. Synergistic interfacial and doping engineering of heterostructured NiCo(OH)_x-Co_yW as an efficient alkaline hydrogen evolution electrocatalyst. *Nano-Micro Lett.* **2021**, *13*, 120. [[CrossRef](#)]
24. Zhang, J.W.; Lv, X.W.; Ren, T.Z.; Wang, Z.; Bandosz, T.J.; Yuan, Z.Y. Engineering heterostructured Ni@Ni(OH)₂ core-shell nanomaterials for synergistically enhanced water electrolysis. *Green Energy Environ.* **2022**, *7*, 1024–1032. [[CrossRef](#)]
25. Jia, Y.; Zhang, L.; Gao, G.; Chen, H.; Wang, B.; Zhou, J.; Soo, M.T.; Hong, M.; Yan, X.; Qian, G.; et al. A heterostructure coupling of exfoliated Ni-Fe hydroxide nanosheet and defective graphene as a bifunctional electrocatalyst for overall water splitting. *Adv. Mater.* **2017**, *29*, 1700017. [[CrossRef](#)]
26. Liu, J.; Yang, Y.; Ni, B.; Li, H.; Wang, X. Fullerene-like nickel oxysulfide hollow nanospheres as bifunctional electrocatalysts for water splitting. *Small* **2017**, *13*, 1602637. [[CrossRef](#)]
27. Rao, Y.; Wang, Y.; Ning, H.; Li, P.; Wu, M. Hydrotalcite-like Ni(OH)₂ nanosheets in situ grown on nickel foam for overall water splitting. *Appl. Mater. Interfaces* **2016**, *8*, 33601–33607. [[CrossRef](#)]
28. Yang, L.; Huang, L.; Yao, Y.; Jiao, L. In-situ construction of lattice-matching NiP₂/NiSe₂ heterointerfaces with electron redistribution for boosting overall water splitting. *Appl. Catal. B Environ.* **2021**, *282*, 119584. [[CrossRef](#)]
29. Wu, T.; Xu, S.; Zhang, Z.; Luo, M.; Wang, R.; Tang, Y.; Wang, J.; Huang, F. Bimetal modulation stabilizing a metallic heterostructure for efficient overall water splitting at large current density. *Adv. Sci.* **2022**, *9*, 2202750. [[CrossRef](#)]
30. Wang, L.; Li, Y.; Xia, M.; Li, Z.; Chen, Z.; Ma, Z.; Qin, X.; Shao, G. Ni nanoparticles supported on graphene layers: An excellent 3D electrode for hydrogen evolution reaction in alkaline solution. *J. Power Sources* **2017**, *347*, 220–228. [[CrossRef](#)]
31. Zhang, J.; Liu, H.; Shi, P.; Li, Y.; Huang, L.; Mai, W.; Tan, S.; Cai, X. Growth of nickel(111) plane: The key role in nickel for further improving the electrochemical property of hexagonal nickel hydroxide-nickel & reduced graphene oxide composite. *J. Power Sources* **2014**, *267*, 356–365.
32. Zhen, W.; Ma, J.; Lu, G. Small-sized Ni(111) particles in metal-organic frameworks with low over-potential for visible photocatalytic hydrogen generation. *Appl. Catal. B Environ.* **2016**, *190*, 12–25. [[CrossRef](#)]
33. Liu, D.; Lu, Q.; Luo, Y.; Sun, X.; Asiri, A.M. NiCo₂S₄ nanowires array as an efficient bifunctional electrocatalyst for full water splitting with superior activity. *Nanoscale* **2015**, *7*, 15122–15126. [[CrossRef](#)] [[PubMed](#)]
34. Zhu, W.; Yue, X.; Zhang, W.; Yu, S.; Zhang, Y.; Wang, J.; Wang, J. Nickel sulfide microsphere film on Ni foam as an efficient bifunctional electrocatalyst for overall water splitting. *Chem. Commun.* **2016**, *52*, 1486–1489. [[CrossRef](#)] [[PubMed](#)]
35. Stern, L.A.; Feng, L.; Song, F.; Hu, X. Ni₂P as a Janus catalyst for water splitting: The oxygen evolution activity of Ni₂P nanoparticles. *Energy Environ. Sci.* **2015**, *8*, 2347–2351. [[CrossRef](#)]
36. Tian, J.; Cheng, N.; Liu, Q.; Sun, X.; He, Y.; Asiri, A.M. Self-supported NiMo hollow nanorod array: An efficient 3D bifunctional catalytic electrode for overall water splitting. *J. Mater. Chem. A* **2015**, *3*, 20056–20059. [[CrossRef](#)]
37. Morales-Guio, C.G.; Stern, L.A.; Hu, X. Nanostructured hydrotreating catalysts for electrochemical hydrogen evolution. *Chem. Soc. Rev.* **2014**, *43*, 6555–6569. [[CrossRef](#)]
38. Armstrong, R.D.; Henderson, M. Impedance plane display of a reaction with an adsorbed intermediate. *J. Electroanal. Chem.* **1972**, *39*, 81–90. [[CrossRef](#)]

Disclaimer/Publisher's Note: The statements, opinions and data contained in all publications are solely those of the individual author(s) and contributor(s) and not of MDPI and/or the editor(s). MDPI and/or the editor(s) disclaim responsibility for any injury to people or property resulting from any ideas, methods, instructions or products referred to in the content.